RSC Advances

PAPER

View Article Online
View Journal | View Issue

Cite this: *RSC Adv.*, 2015, **5**, 63304

A high capacity $MnFe_2O_4$/rGO nanocomposite for Li and Na-ion battery applications†

Pratap Kollu,*[a] P. Ramesh Kumar,[b] Chella Santosh,[c] Do Kyung Kim*[b] and Andrews Nirmala Grace*[c]

Received 15th June 2015
Accepted 17th July 2015

DOI: 10.1039/c5ra11439j

www.rsc.org/advances

A porous $MnFe_2O_4$/reduced graphene oxide (rGO) nanocomposite with high storage capacity was prepared by a hydrothermal method. The $MnFe_2O_4$/rGO nanocomposite sample was characterized by X-ray diffraction, Raman spectroscopy, scanning electron microscopy and high resolution transmission electron microscopy. The electrochemical characteristics with lithium as well as sodium were studied using cyclic voltammetry and a battery cycle tester. In this work, apart from the lithium storage, the sodium storage ability of the spinel type $MnFe_2O_4$ as an anode is demonstrated for the first time. The prepared $MnFe_2O_4$/rGO composite with sodium alginate binder shows a highly stable capacity of 905 mA h g^{-1} *versus* Li/Li^+ and 258 mA h g^{-1} *versus* Na/Na^+ at 0.1C rate. The enhancement in capacity and excellent cycleability of the $MnFe_2O_4$/reduce graphene oxide nanocomposite is due to constrained volume expansion during conversion reactions and enhancement of electrical conductivity.

1. Introduction

In recent times, there has been an incredible increase in the use of lithium ion batteries due to their practical applications in electronic devices, hybrid electric vehicles and all types of electric vehicles.[1–5] In order to find an alternative to lithium energy storage systems, researchers have focused on sodium ion batteries. Sodium is very cheap and abundant in the earth's crust, which makes it the most advantageous element for battery applications after lithium. Furthermore, its interaction chemistry is similar to lithium. These days, the most common anode materials used in secondary ion batteries are carbon materials. The drawback of using carbon materials as anodes is that they lead to a lower reversible storage capacity that cannot meet the growing demands of high storage capacity of secondary batteries.[6] It has thus become imperative to develop an electrode material with low cost, long life, high storage capacity and safety.[7–9] One of the promising materials having high performance as anode materials for secondary ion batteries is transition metal oxides (TMO). The TMO based materials has high capacity as compared with the commercially used graphite material (*e.g.*, 1007 mA h g^{-1} of Fe_2O_3; 890 mA h g^{-1} of Co_3O_4; 755 mA h g^{-1} of MnO; 717 mA h g^{-1} for NiO).[10,11] Also, binary metal oxides also called as spinel ferrites with the general formula MFe_2O_4 (M = Mn, Co, Ni, Zn or Mg) are very fascinating materials due to their interesting electrical and magnetic properties with high thermal and chemical stabilities.[12] Manganese ferrite ($MnFe_2O_4$) one of the ferrite families is grown as various morphologies such as nanocrystals,[13] nanocubes[14] and hollow spheres.[15] Manganese ferrite stores through the conversion reaction mechanism ($MnFe_2O_4 + 8X^+ + 8e^- - Mn + 2Fe + 4X_2O$: X = Li & Na) and it has high theoretical capacity of 928 mA h g^{-1}, which is much higher than carbon anode (375 mA h g^{-1}). The TMO materials show poor electrochemical performances due to low electronic conductivity. To overcome this problem, doping of high electronic conducting carbon forms to achieve enhanced electrochemical properties is essential.

Besides, graphene based nanocomposites as anodes for rechargeable lithium ion batteries have been extensively investigated, such as graphene–metal composite,[16] graphene–metal oxides[17] and graphene–sulfur composites.[18] The decoration of nanoparticles into the graphene sheets will generate a porous network, providing an outstanding electron-conducting and ion-transporting pathway.[19,20] The theoretical capacity of graphene is 744 mA h g^{-1}, which is twice than that of graphite materials. In case of sodium ion battery, Fe_2O_3/graphene sheet composites,[21] and MoS_2/carbon nanofibers[22] *etc.*…, were used as anode materials.[23] Thus, graphene based nanocomposite materials will have enhanced electrochemical performances, particularly charging/discharging process and rate capabilities. In present work, manganese ferrite incorporated in graphene sheets was prepared *via* solvothermal process. The prepared

[a]*Thin Film Magnetism Group, Cavendish Laboratory, Department of Physics, University of Cambridge, J J Thomson Avenue, Cambridge CB3 0HE, UK. E-mail: pk419@cam.ac.uk*

[b]*Department of Materials Science and Engineering, Korea Advanced Institute of Science and Technology (KAIST), Daejeon 305-701, Republic of Korea. E-mail: dkkim@kaist.ac.kr; Fax: +82-42-350-3310; Tel: +82-42-350-4118*

[c]*Centre for Nanotechnology Research, VIT University, Vellore-632014, India. E-mail: anirmalagrace@vit.ac.in*

† Electronic supplementary information (ESI) available: TGA, CV and cyclic stability for pure $MnFe_2O_4$. See DOI: 10.1039/c5ra11439j

materials were characterized using XRD, Raman, SEM and TEM techniques. The composite was further tested as anode for lithium as well as sodium ion battery applications and results showed that it exhibited high storage capacity and excellent cyclic stability.

2. Experimental

2.1 Synthesis of $MnFe_2O_4$/rGO composite

Graphene oxide is primary precursor to synthesis the reduced graphene oxide and manganese ferrite nanocomposite ($MnFe_2O_4$/rGO), which was prepared from natural graphite by a modified Hummer's method.[24] Manganese ferrite nanocomposite was synthesized from our previous work.[25] In a typical procedure, 300 mg of graphene oxide, 3 mmol of manganese chloride ($MnCl_2 \cdot 4H_2O$) and 6 mmol of ferric chloride ($FeCl_3 \cdot 6H_2O$) were mixed and dissolved in an appropriate amount of ethylene glycol followed by ultrasonication for more than 2 h. Then the mixture was subjected to stirring by adding sodium acetate and polyethylene glycol about for a certain time. The product was sealed in Teflon coated hydrothermal bomb and kept in hot-air oven at 200 °C for 10 h. Finally, after reaching to room temperature, the product was separated by centrifugation for several times in water and ethanol followed by drying at 60 °C.

2.2 Characterization

X-Ray diffraction patterns (XRD) were recorded on a Rigaku Miniflex using the Cu Kα radiation ($\lambda = 1.5406$ Å) over 2θ range from 10–80°. The microscopic feature of the samples was characterized by field-emission scanning electron microscopy (SEM) (Hitachi S-4800) and high-resolution transmission electron microscopy (HR-TEM) with Energy Dispersive Spectrometer (EDS) (JEOL-2000EX, JEOL, Tokyo, Japan) operated at 120 kV. Raman measurements were carried out in the back scattered geometry using an (He–Ne laser) laser excitation source emitting at 514 nm with 20 mW power coupled with an ARAMIS (Horiba Jobin Yvon, France) micro-Raman spectrometer. Elemental analysis (EA) experiment was carried out by using Thermo Scientific Flash 2000 Series element analyser. Thermogravimetric (TG) analysis was carried out on Q600 (TA Instruments, USA) at a heating rate of 5 °C min^{-1} in air (200 ml min^{-1}).

2.3 Electrochemical measurement

Electrochemical studies of the synthesized $MnFe_2O_4$/rGO nanospheres were carried out in CR2032 type cells. The electrode composite consists of 70% active material, 20% Super P carbon and 10% Na-alginate in DI water solvent. The above mixture was grounded properly to form slurry. The slurry was coated on to a Cu-foil and dried at room temperature overnight. The dried Cu-foil was cut into circular electrode disks. The CR2032 type cells were assembled in Argon filled glove box by using celgard 2400 as separator. Lithium and sodium metals were used as counter electrodes. 1 M $LiPF_6$ in ethylene carbonate (EC) and diethyl carbonate (DEC) (1 : 1 v/v%) was used as electrolyte for lithium ion batteries. In case of sodium, 1 M $NaClO_4$ in propylene carbonate (PC) and fluoroethylene carbonate (FEC) (98 : 2 v/v%) was used as electrolyte. The galvanostatic charge–discharge studies were carried out at different C-rates in the voltage range of 3–0.002 V using a battery cycle tester (Wonatec, Korea).

3. Results and discussion

3.1 Structural analysis

The XRD diffraction pattern of natural graphite powder, graphene oxide and $MnFe_2O_4$/rGO along with JCPDS data were shown in Fig. 1. From Fig. 1b, natural graphite flake shows a lattice planes of (002), (101) and (004) at 26.4°, 42.5° and 54.6° respectively with 3.38 Å spacing between the layers. As seen from the pattern after oxidation, graphitic peak (002) disappeared and a new peak at 11.08° with a lattice structure of (001) of GO was observed (Fig. 1c), whereas for GO the spacing between the layers were 8.2 Å with a lattice plane at 11.08° suggesting that natural graphite flakes were converted into rGO. In the XRD pattern of $MnFe_2O_4$/rGO (Fig. 1d), the disappearance of the peak at 11.08° confirms the detachment of oxygen groups and reduction of graphene oxide to graphene nanosheets. Diffraction peaks at 2θ values of 18.03°, 30.18°, 35.46°, 43.02°, 53.81°, 56.89°, 62.55°, 70.20° and 73.3° were observed which correspond to (111), (220), (311), (400), (422), (333), (440), (533) and (622) crystal planes of $MnFe_2O_4$ in accordance with the standard JCPDS no. 742403. The peaks were broad indicating the nanocrystalline nature of the material. Under these experimental conditions, no other diffraction peaks were obtained, which indicates that the prepared material is of high purity.

For the reference, pure $MnFe_2O_4$ XRD patterns along with JCPDS data was shown in Fig. S1.† Raman spectroscopy is one of the techniques, to know the defects in the sp^2 carbon materials. As shown in the Fig. 2, the Raman spectra of as-prepared material $MnFe_2O_4$/rGO have peaks at 1340, 1595, 2680 and 2947 cm^{-1} are assigned to D, G, 2D and D + G-bands respectively and a weak peak at 615 cm^{-1} was assigned to the $MnFe_2O_4$ nanoparticles.[26]

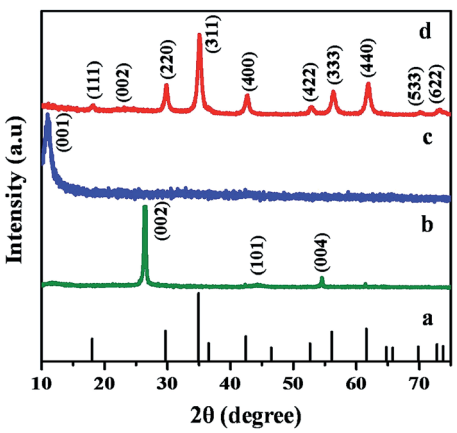

Fig. 1 X-Ray diffraction pattern of (a) $MnFe_2O_4$ JCPDS data, (b) graphite, (c) graphene oxide and (d) $MnFe_2O_4$/rGO nanocomposite.

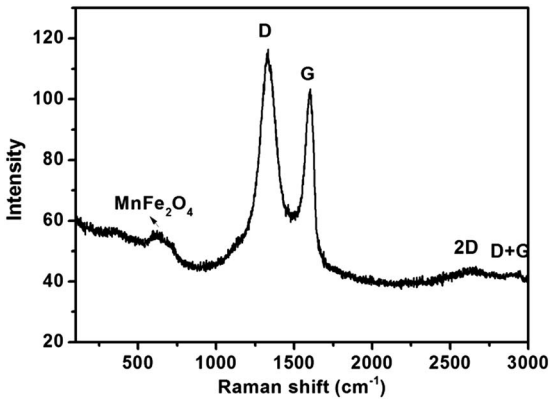

Fig. 2 Raman spectra of as-prepared material $MnFe_2O_4$/rGO.

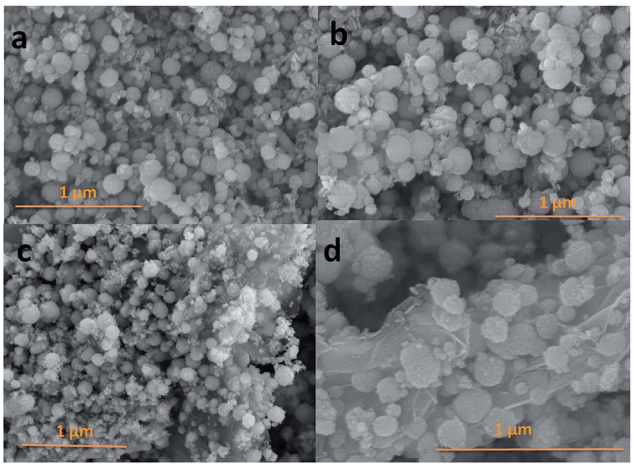

Fig. 3 FE-SEM images of (a & b) the pure $MnFe_2O_4$ and (c & d) as-prepared material $MnFe_2O_4$/rGO.

3.2 Morphological & thermo-gravimetric analysis

The surface morphology and particle size of the as-prepared $MnFe_2O_4$/rGO nanocomposite were further analyzed by FE-SEM and HR-TEM. From the FE-SEM images as shown in Fig. 3, it was observed that the $MnFe_2O_4$ nanoparticles were well decorated as homogeneous spherical particles onto the graphene sheets and the estimated cluster size was ~130 nm. Fig. 3c and d shows the SEM images of the $MnFe_2O_4$/rGO nanocomposite in different magnifications. From Fig. 3d, the $MnFe_2O_4$ nanoclusters were sandwich between graphene sheets, which is good evidence for the stable electrode operations during the conversion reaction.[27] Structure of the $MnFe_2O_4$/rGO nanocomposite was further investigated by HR-TEM. HR-TEM images of pure porous $MnFe_2O_4$ nanostructures at different magnifications are shown in Fig. 4, which indicated the formation of agglomerated clusters made up off very small nano sized particles with ~120 nm in diameter, which is close that observed from FE-SEM. The SAED patterns were recorded and Debye-Scherrer rings were obtained. These are shown in Fig. 4d and represented as (111), (220), (311), (400), (422), (333), (440), (533) and (622) lattice planes, which are supported by the XRD analysis. Furthermore, from elemental analysis, the carbon content in this composite is 19 wt%. Hence it is confirmed from the above analysis that the solvothermal route offered a homogeneous synthesis of the composite.

Furthermore, thermo-gravimetric analyses of the composite were carried out in air to know the phase changes and decomposition details. $MnFe_2O_4$/rGO composite was heated to 1000 °C at a rate of 5 °C min^{-1} and the corresponding TG and DTA curves for $MnFe_2O_4$/rGO composite is given in Fig. S2.† The TGA measurement identifies the weight loss of the materials from 35 °C to 1000 °C. The weight loss below 100 °C is ascribed to be desorption of physically adsorbed moisture. Furthermore, weight loss above 150 °C is due to decomposition of ethylene glycol, whereas from 500–800 °C, a plateau is observed which could be due to the partial decomposition of the sample to form monophasic $MnFe_2O_4$.[28,29] After 750 °C, there is an abrupt decrease in weight (%), which could be due to burning of graphene. This temperature is slightly higher as it is in the form of composite with $MnFe_2O_4$.[30] From Fig. S2,† the loading percentage of graphene was calculated from TGA of $MnFe_2O_4$/rGO. As observed, the decomposition of graphene starts after 750 °C with a corresponding weight loss of 21% (calculated from the difference in weight% in the declination of the weight (%) curve on the left *y*-axis after 750 °C). Thus taking into consideration the weight loss due to absorbed moisture, EG molecules and graphene, the loading of $MnFe_2O_4$ is 79%.

3.3 Electrochemical analysis

The cyclic voltammetry of $MnFe_2O_4$/rGO *versus* Li & Na for twenty cycles between 3 to 0.002 V at a scan rate of 0.2 mV s^{-1} are shown in Fig. 5a and b respectively. From Fig. 5a, in the first cycle, a large cathodic peak located around 0.5 V *vs.* Li/Li^+ can be associated with the reduction reactions of Fe^{3+} and Mn^{2+} with Li and the formation of Li_2O during the first discharge process. In the subsequent cathodic scans, $MnFe_2O_4$/rGO nanoclusters show a cathodic peak and anodic peak at 0.7 V and 1.6 V *vs.*

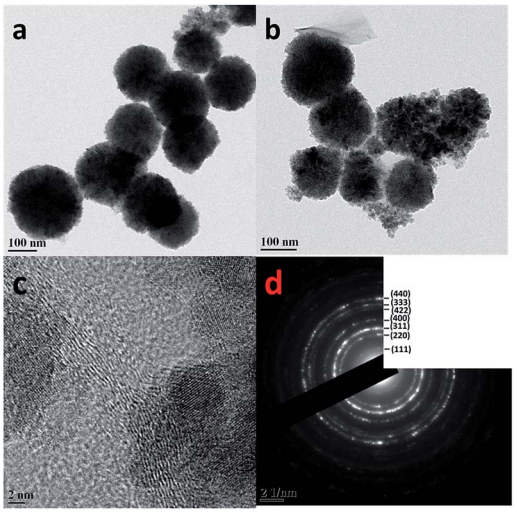

Fig. 4 HR-TEM images of $MnFe_2O_4$/rGO with SADE pattern.

Li/Li^+ and can be attributed to the reductive reaction of Fe_2O_3 and MnO to Fe and Mn metal, respectively. The $MnFe_2O_4$/rGO composites show all redox reaction peaks for $MnFe_2O_4$ nanoparticles. After the first cycle, the intensity of redox peaks remains constant which indicates the electrode stability.[31] From Fig. S1,† the cyclic voltammogram of pure $MnFe_2O_4$ intensity of peaks changes with cycle numbers, which indicates lower stability against lithium. Fig. 5b shows the CV profile for $MnFe_2O_4$/rGO composites *versus* Na/Na^+. In Fig. 5b, the observed anodic peaks at 1.6 and 1.85 V correspond to oxidation of Fe^0 to Fe^{3+} and Mn^0 to Mn^{2+}.[32] The broad cathodic peak centered at 0.75 V is attributed to the reduction reactions of Fe^{3+} and Mn^{2+} with Na and the formation of Na_2O during the discharge process.

The $MnFe_2O_4$/rGO was showing good rate capability and cycling stability due to the 2D graphene structure which will provide the conductive path for electron transportation and also it will accommodate the volume expansion while charging/discharging. Furthermore, alginate binder has better adhesive nature with the current collector and anode material during conversion reaction. The alginate binder effect on one of the spinel transition metal oxide has been demonstrated in our previous reports.[33] Hence, the capacity fading is minimized in the lithium ion battery fabricated with $MnFe_2O_4$/rGO anode and alginate binder. This is reflected in the discharge capacity retention up to few numbers of cycles.

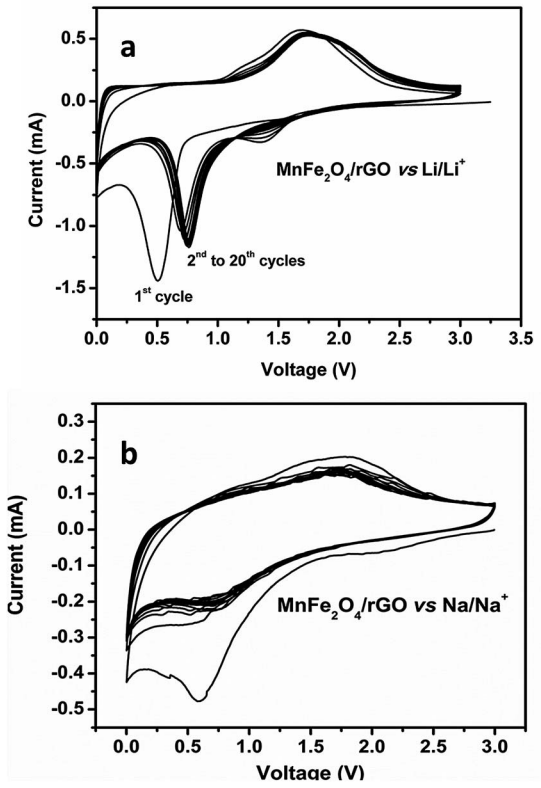

Fig. 5 Cyclic voltammetry plots for the (a) $MnFe_2O_4$/rGO *vs.* Li/Li^+ and (b) $MnFe_2O_4$/rGO *vs.* Na/Na^+ composites.

Fig. S4a and b† show the voltage profile and charge/discharge capacity *vs.* cycle number plots for the pure $MnFe_2O_4$ electrode at 0.1C rate. From Fig. S4a,† pure $MnFe_2O_4$ electrode delivers discharge capacity of 990 mA h g^{-1} at first discharge. The capacity fading is observed when the number of cycle is increasing. A deep fall in the discharge capacity from the initial value to 405 mA h g^{-1} in the 30th cycle is observed. This lower cyclic stability is reflected the previous mentioned CV results. The observed low stable cyclability in pure $MnFe_2O_4$ electrodes *versus* Li is might be due to low electronic conductivity and nano sized particles in cluster dissolution in electrolyte while charging–discharging.

The cycleability and charge discharge curves for the $MnFe_2O_4$/rGO *versus* Li/Li^+ material are shown in Fig. 6. From Fig. 6, the $MnFe_2O_4$/rGO has delivered stable capacity of 905 mA h g^{-1} at 0.1C rate for 30 cycles with excellent coulombic efficiency. The $MnFe_2O_4$/rGO composites presented the extra 1st discharge capacity, is due to the reversible formation and decomposition of polymeric gel-like films on the active particles.[34,35] The significance of our $MnFe_2O_4$/rGO composite was its increased capacity at 0.1C and cyclic stability compared to recently reported Co_3O_4@graphene composites,[10] Fe_3O_4/rGO,[36] and $NiFe_2O_4$ nanoparticles.[37] The enhancement of electrochemical properties of $MnFe_2O_4$/rGO *versus* Li/Li^+ is can be due to the better electronic conductivity network. The discharge profile *versus* sodium was shown in Fig. 7. From Fig. 7a, the $MnFe_2O_4$/rGO *vs.* Na/Na^+ has delivered stable capacity of 258 mA h g^{-1} at 0.1C rate for 50 cycles. Furthermore, we are the first group who demonstrated $MnFe_2O_4$/rGO composite as an anode for sodium ion batteries. From Fig. 6 and 7, two things are clearly observed when the $MnFe_2O_4$/rGO composite is using as anode for Li and Na-ion batteries. First, the shape difference in charge–discharge curves. The charge–discharge curves of $MnFe_2O_4$/rGO *versus* Li/Li^+ has shows one voltage plateau at 0.8 V, but $MnFe_2O_4$/rGO *versus* Na/Na^+ charge–discharge curves does not shows any plateau region. Second, capacity difference, $MnFe_2O_4$/rGO composite has high Li storage capacity than Na capacity. The above mentioned two differences between Li and Na-ion batteries are may be due to the low ionic diffusivity of Na-ion.

The voltage *vs.* cycle number and discharge profile for the battery fabricated with $MnFe_2O_4$/rGO at different current rates are shown in Fig. 8a–d respectively. From Fig. 8a and b, discharge capacity of the anode *versus* Li/Li^+ decreases to 720, 580, 320, 160 and 60 mA h g^{-1} when current rate increased to 1C (920 mA g^{-1}), 2C (1840 mA g^{-1}), 5C (4600 mA g^{-1}) and 10C (9200 mA g^{-1}), respectively. From Fig. 8c and d, discharge capacity of the anode *versus* Na/Na^+ with different current rates are 98 mA h g^{-1} (920 mA g^{-1}), 58 mA h g^{-1} (1840 mA g^{-1}), 22 mA h g^{-1} (4600 mA g^{-1}) and 8 mA h g^{-1} (9200 mA g^{-1}). The high rate capability and good reversibility are due to the good electronic conductivity, higher surface area and excellent adhesive properties of 2D graphene and alginate binders.[38] The cross linking hydrocarbon chain and swelling nature of alginate binder, maintains good electrical contact between the current collector and anode material upon continuous conversion.

Xuefeng *et al.*, successfully demonstrated reaction mechanism of $MnFe_2O_4$/graphene composites *versus* Li/Li^+ using *ex*

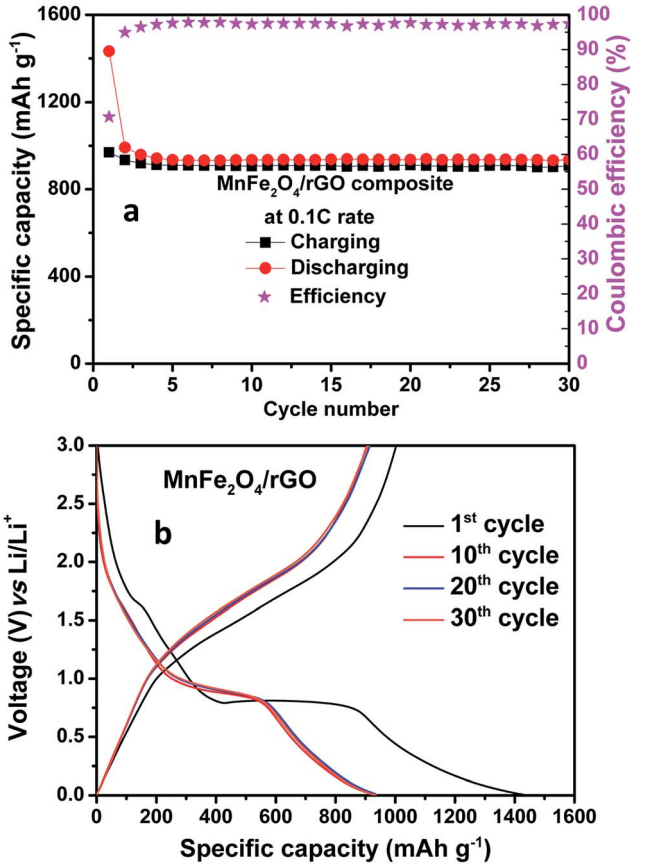

Fig. 6 (a) Cyclic stability and (b) charge–discharge curves for the $MnFe_2O_4$/rGO composites *vs.* Li/Li^+.

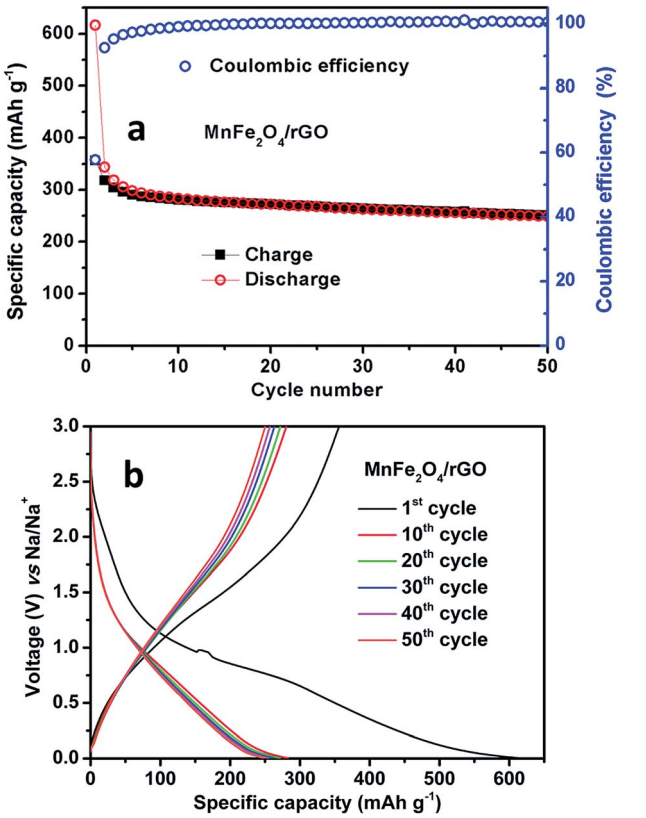

Fig. 7 (a) Cycling stability and (b) charge–discharge curves for the $MnFe_2O_4$/rGO composites *vs.* Na/Na^+.

situ XRD and TEM analysis.[32] Here, first time the path of reaction mechanism of $MnFe_2O_4$/graphene composites *versus* Na/Na^+ during discharging and charging was observed by using *ex situ* TEM for the 1st discharge and 1st charge electrodes. Fig. 9a and b shows the *ex situ* TEM image and SAED patterns for the 1st discharge $MnFe_2O_4$/rGO composite electrode *versus* Na/Na^+. From Fig. 9a and b, the retention of morphology and the inter planer distance are derived by measuring the distance between bright rings about the center. The obtained, inter planer distance values are matched to the Miller indices of pure Fe, Mn and Na_2O. The *ex situ* TEM results for the fully charged $MnFe_2O_4$/rGO composite electrode are shown in Fig. 9c and d. In Fig. 9c, the morphology is totally changes from nanoclusters to tiny metal oxide particles which are bounded in graphene network. SAED patterns of fully charged electrode in Fig. 9d and it is observed that the formation of Fe_2O_3 and MnO at charge state. Hence, it is proved that the Fe, Mn metals and sodium oxide formed at discharge state and the formation of Fe_2O_3 and MnO at charge state. Furthermore, we have taken *ex situ* XRD for the 1st discharge and 1st charge electrodes, but it is very hard to find corresponding peaks in X-ray diffraction. The XRD patterns for 1st discharge and 1st charge electrodes along with their JCPDS data are shown Fig. S3.† Hence, it is confirmed that formation of Fe_2O_3 and MnO at charged state using *ex situ* TEM results, which the direct evidence for conversion reaction mechanism as is proposed in earlier section.

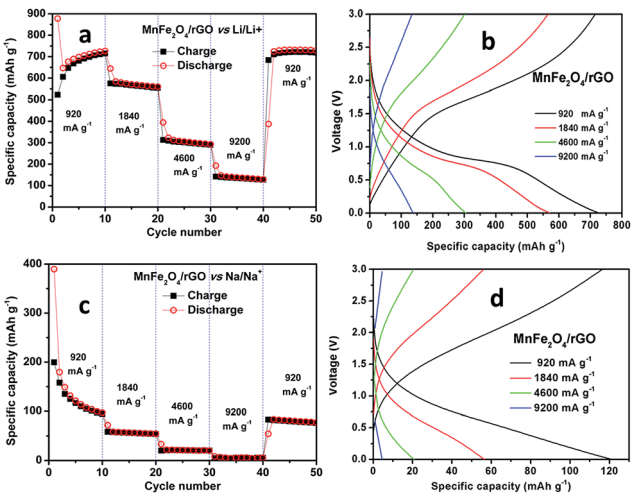

Fig. 8 (a & c) Rate capability and (b & d) charge–discharge curves at different rates for the $MnFe_2O_4$/rGO composites *vs.* Li/Li^+ and Na/Na^+ respectively.

Fig. 10a–d, show the Nyquist plots for the $MnFe_2O_4$/rGO composite electrode at discharging and charging states *versus* Li and Na. In Fig. 10a and b, we can observe that there is one depressed semicircle with spike in the lower frequency side *versus* Na. The observed depressed semicircle was fitted by using an $R_{(SF+CT)}$ combination. From the first dispersed

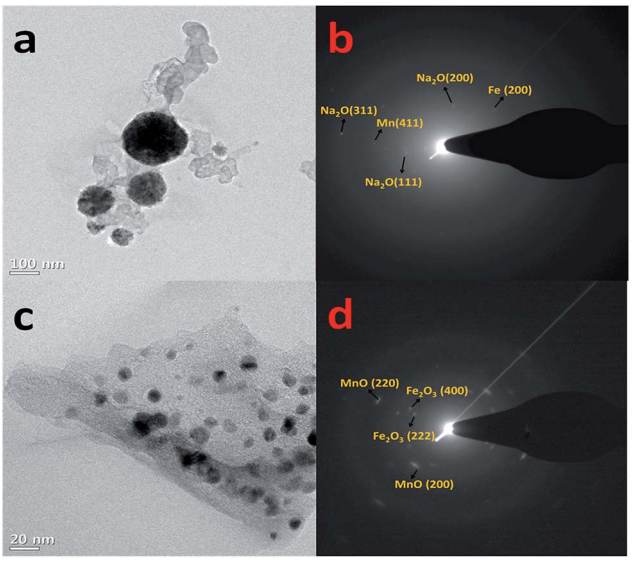

Fig. 9 *Ex situ* TEM results of $MnFe_2O_4$/rGO composites *vs.* Na/Na^+ electrodes (a and b) images and SAED patterns for 1st discharge state and (c and d) image and SAED patterns for 1st charge state.

Table 1 R_e, R_{CT}, R_{SF}, and W_d values of $MnFe_2O_4$/rGO electrode *versus* Li and Na during the 1st discharge–charge cycles at various voltages

Voltage	Li/Li^+			Na/Na^+			
	R_e	$R_{(SF+CT)}$	W_d	R_e	R_{SF}	R_{CT}	W_d
Discharging	4.66	80	0.44	4.75	455	3842	0.57
OCV							
2	4.69	102	0.799	5.49	551	2059	0.61
1.2	4.72	82	0.83	6.02	524	1517	0.7
0.8	4.84	151	0.85	6.32	1154	461	0.75
0.4	4.86	232	0.83	6.072	385	881	0.77
0.02	5.03	243	0.83	5.13	258	621	0.49
Charging	5.01	251	0.83				
0.6				5.66	237	342	0.59
1.2	5.043	218	0.84	5.71	603	185	0.77
2	5.00	210	0.85	5.8	142	3275	0.42
3	5.27	141	0.89	6.31	633	184	0.73

semicircle, $R_{(SF+CT)}$ resistance values could be estimated from fitted data and presented in Table 1. The value of $R_{(SF+CT)}$ increasing and decreasing during discharging and charging might be due to the solid electrolyte interface (SEI) formation/partial dissolution/re-formation.[39] Fig. 10c and d, shows the two distinct semi circles, which are belongs to the R_{SF} and R_{CT} and varying during the charging and discharging states *versus* Na. From Fig. 10c and d, it is observed that the values of R at OCV (initial point of discharging state) and 3 V (final point of charging state) are almost equal. Hence, it is confirmed that the SEI between electrolyte and $MnFe_2O_4$/rGO composite is stable during the discharging and charging. Furthermore, nano-sized porous structures with 2D graphene network offer good charge transfer kinetics due to their high surface to volume ratio.

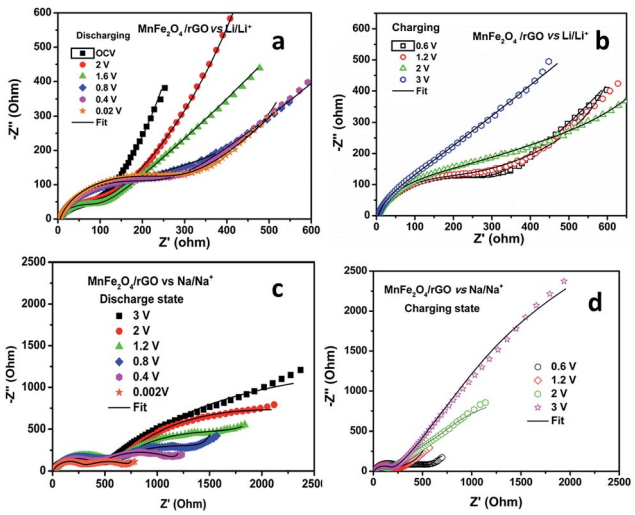

Fig. 10 Nyquist plots for the $MnFe_2O_4$/rGO (a & b) *vs.* Li/Li^+ and (c & d) *vs.* Na/Na^+ during the charging–discharging.

4. Conclusions

Spinel manganese ferrite/reduce graphene oxide ($MnFe_2O_4$/rGO) nanocomposite was synthesized from natural graphite by a modified Hummer's method. XRD and Raman results confirmed the formation of $MnFe_2O_4$/rGO phase and structure respectively. Micro structural analysis was done using SEM and HRTEM, which showed the uniform dispersion of ferrites in graphene sheet network. The $MnFe_2O_4$/rGO composites delivers a high stable maximum discharge capacity of 905 mA h g^{-1} *vs.* Li/Li^+ and 258 mA h g^{-1} *vs.* Na/Na^+ at 0.1C rate. Here, Na-alginate binder provided a strong interaction between active material and current collector; further graphene sheets gave the enough void space for the volume expansion during the conversion reaction, act as a barrier to avoid active material dissolution and also it will enhance the electrical conductivity of nanocomposite. Results demonstrated that the $MnFe_2O_4$/rGO composite material with alginate is a potential anode material for next generation rocking chair battery applications.

Acknowledgements

Dr Pratap Kollu gratefully acknowledges Newton International Fellowship, The Royal Society and The British Academy, UK and DST-INSPIRE Faculty award, India. Prof. D. K. Kim acknowledges financial support from the Program to Solve Climate Changes (NRF-2010-C1AAA001-2010-0029031) of Korea (NRF) funded by the Ministry of Science, ICT & Future Planning. Authors acknowledge SAIF, Central surface analytical facility of IIT Bombay.

References

1 P. Poizot, S. Laruelle, S. Grugeon, L. Dupont and J. M. Tarascon, *Nature*, 2000, **407**, 496–499.

2 Y. J. Lee, H. Yi, W. J. Kim, K. Kang, D. S. Yun, M. S. Strano, G. Ceder and A. M. Belcher, *Science*, 2009, **324**, 1051–1055.
3 H. L. Wang, L. F. Cui, Y. A. Yang, H. S. Casalongue, J. T. Robinson, Y. Y. Liang, Y. Cui and H. Dai, *J. Am. Chem. Soc.*, 2010, **132**, 13978–13980.
4 P. G. Bruce, B. Scrosati and J. M. Tarascon, *Angew. Chem., Int. Ed.*, 2008, **47**, 2930–2946.
5 Z. Li, X. Z. Zhan, D. Gao, Q. Xiao and G. Lei, *Electrochim. Acta*, 2010, **55**, 4594–4598.
6 H. Zhao, Z. Zheng, K. W. Wong, S. Wang, B. Huang and D. Li, *Electrochem. Commun.*, 2007, **9**, 2606–2610.
7 V. Palomares, P. Serras, I. Villaluenga, K. B. Hueso, J. Carretero-Gonzalez and T. Rojo, *Energy Environ. Sci.*, 2012, **5**, 5884–5901.
8 X. Su, Q. L. Wu, X. Zhan, J. Wu, S. Wei and Z. Guo, *J. Mater. Sci.*, 2012, **47**, 2519–2534.
9 H. Pan, Y. S. Hu and L. Chen, *Energy Environ. Sci.*, 2013, **6**, 2338–2360.
10 B. Li, H. Cao, J. Shao, G. Li, M. Qu and G. Yin, *Inorg. Chem.*, 2011, **50**, 1628–1632.
11 Y. Wang, X. Yu, S. Xu, J. Bai, R. Xiao, Y. S. Hu, H. Li, X. Q. Yang, L. Chen and X. Huang, *Nat. Commun.*, 2013, **4**, 2365–2371.
12 S. Maensiri, M. Sangmanee and A. Wiengmoon, *Nanoscale Res. Lett.*, 2009, **4**, 221–228.
13 Q. Song, Y. Ding, Z. L. Wang and Z. J. Zhang, *Chem. Mater.*, 2007, **19**, 4633–4638.
14 L. Wang, X. Wang, J. Luo, B. N. Wanjala, C. Wang, N. A. Chernova, M. H. Engelhard, Y. Liu, I. T. Bae and C. J. Zhong, *J. Am. Chem. Soc.*, 2010, **132**, 17686–17689.
15 P. Hu, L. Yu, A. Zuo, C. Guo and F. Yuan, *J. Phys. Chem. C*, 2009, **113**, 900–906.
16 L. Tian, Q. Zhuang, J. Li, C. Wu, Y. Shi and S. Sun, *Electrochim. Acta*, 2012, **65**, 153–158.
17 S. Chen, Y. Wang, H. Ahn and G. Wang, *J. Power Sources*, 2012, **216**, 22–27.
18 L. Ji, M. Rao, H. Zheng, L. Zhang, Y. Li, W. Duan, J. Guo, E. Cairns and Y. Zhang, *J. Am. Chem. Soc.*, 2011, **133**, 18522–18525.
19 C. H. Lim, A. G. Kannan, H. W. Lee and D. K. Kim, *J. Mater. Chem. A*, 2013, **1**, 6183–6190.
20 Y. Zuo and Y. Wang, *ACS Nano*, 2011, **5**, 8108–8114.
21 Z. Jian, B. Zhao, P. Liu, F. Li, M. Zheng, M. Chen, Y. Shi and H. Zhou, *Chem. Commun.*, 2014, **50**, 1215–1217.
22 C. Zhu, X. Mu, P. A. van Aken, Y. Yu and J. Maier, *Angew. Chem., Int. Ed.*, 2014, **53**, 2152–2156.
23 P. Ramesh Kumar, Y. H. Jung, K. K. Bharathi, C. H. Lim and D. K. Kim, *Electrochim. Acta*, 2014, **146**, 503–510.
24 W. S. Hummers and R. E. Offeman, *J. Am. Chem. Soc.*, 1958, **80**, 1339.
25 C. Santhosh, J. Ann Miriam, T. Malathy, M. Saranya, R. Ramachandran, S. Felix, T. Mudaliar Vanchinathan, V. Velmurugan and A. Nirmala Grace, *Nanosci. Nanotechnol.–Asia*, 2013, **3**, 120–126.
26 J. Zhu, T. Zhu, X. Zhou, Y. Zhang, X. W. Lou, X. Chen, H. Zhang, H. H. Hng and Q. Yan, *Nanoscale*, 2011, **3**, 1084–1089.
27 Y. Shi, S. L. Chou, J. Z. Wang, H. J. Li, H. K. Liu and Y. P. Wu, *J. Power Sources*, 2013, **244**, 684–689.
28 P. Guo, G. Zhang, J. Yu, H. Li and X. S. Zhao, *Colloids Surf., A*, 2012, **395**, 168–174.
29 N. N. Mallikarjuna, A. Lagashetty and A. Venkataraman, *J. Therm. Anal. Calorim.*, 2003, **74**, 819–826.
30 Y. Feng, T. He and N. A. Vante, *ECS Trans.*, 2008, **11**, 67–72.
31 Y. J. Mai, D. Zhang, Y. Q. Qiao, C. D. Gu, X. L. Wang and J. P. Tu, *J. Power Sources*, 2012, **216**, 201–207.
32 X. Yinglin, Z. Jiantao, T. Liqi, L. Bo, H. Qianyan, Y. Chao and Q. Xuefeng, *Phys. Chem. Chem. Phys.*, 2013, **15**, 3939–3945.
33 P. Ramesh Kumar, P. Kollu, C. Santhosh, K. E. V. Rao, D. K. Kim and A. N. Grace, *New J. Chem.*, 2014, **38**, 3654–3661.
34 L. Su, Y. Zhong and Z. Zhou, *J. Mater. Chem. A*, 2013, **1**, 15158–15166.
35 Y. Shi, J. Z. Wang, S. L. Chou, D. Wexler, H. J. Li, K. Ozawa, H. K. Liu and Y. P. Wu, *Nano Lett.*, 2013, **13**, 4715–4720.
36 S. Bhuvaneswari, P. M. Pratheeksha, S. Anandan, D. Rangappa, R. Gopalan and T. N. Rao, *Phys. Chem. Chem. Phys.*, 2014, **16**, 5284–5294.
37 P. Ramesh Kumar and S. Mitra, *RSC Adv.*, 2013, **3**, 25058–25064.
38 S. Mitra, P. S. Veluri, A. Chakraborthy and R. K. Petla, *ChemElectroChem*, 2014, **1**, 1068–1074.
39 Y. Sharma, N. Sharma, G. V. Subba Rao and B. V. R. Chowdari, *Solid State Ionics*, 2008, **179**, 587–597.

